Intermodulation Analysis of Dual-Gate FET Mixers

Junghyun Kim, *Student Member, IEEE,* and Youngwoo Kwon, *Member, IEEE*

***Abstract*—A detailed intermodulation analysis of dual-gate FET (DG-FET) mixers is presented. The analysis method is based on a large-signal/small-signal analysis using time-varying Volterra-series methods. The analysis program allows one to probe the internal nodes of DG-FETs to evaluate the nonlinear current components. Therefore, it helps physical understanding of intermodulation distortion (IMD) mechanisms in DG-FET mixers. The program was used to identify the major sources of IMD generation. It was found from the analysis that the nonlinearities due to the output conductance (G_{d3} and G_{d2}) of the lower common-source FET were most responsible for IMD generation. The impact of the upper common-gate FET on IMD generation was also found to be nonnegligible, especially at high local oscillator (LO) power levels. The analysis also predicted the presence of IMD "sweet spots" using bias optimization, which was experimentally proved by the fabricated mixers at X- and Ka-bands. The optimized X-band hybrid mixer showed measured intermodulation characteristics ($\mathrm{OIP}_3 \sim 13.6$ dBm) comparable to those of the resistive mixers ($\mathrm{OIP}_3 \sim 15.3$ dBm) with low LO and dc power conditions. Very good agreement between the measurement and simulation was found for the two mixers using different types of transistors, which validates our analysis method and supports the general adequacy of our approach. This paper presents a comprehensive IMD analysis and design methodology for DG-FET mixers, and shows that well-designed DG-FET mixers are very promising for modern monolithic applications requiring high linearity.**

***Index Terms*—Dual-gate FET, HEMT, intermodulation, mixer, MMIC.**

I. Introduction

MODERN digital communication systems require high linearity, characterized by low intermodulation distortion (IMD), in order to reduce the error rates. The intermodulation performance of a front-end receiver is often limited by that of the mixer. This is due to the fact that the mixer must handle the largest RF signal, and the IMD performance of a mixer is usually worse than that of other components. For this reason, accurate intermodulation analysis of the mixers has recently become a critical part of the receiver analysis and design.

The intermodulation analysis of diode mixers has been available since the late 1980s [1]. On the contrary, few works have been published on the IMD analysis of FET mixers, except for the case of FET resistive mixers [2]–[5], which offer good linearity characteristics. The wide availability of IMD analysis of FET resistive mixers is due to the fact that they are essentially passive mixers and, thus, the analysis method is basically identical to that of the diode mixers. In the case of active FET mixers, few studies have been available. Peng *et al.* [6] recently presented an intermodulation analysis of single-gate FET mixers using the large- and small-signal analysis method pioneered by Maas to calculate the IMD of diode mixers [1]. However, the analysis was limited to the single-gate common-source FET (CS-FET) mixers in [6].

Among various mixer types using FETs, dual-gate FET (DG-FET) mixers are of particular interest for monolithic applications. DG-FETs offer on-chip RF/local oscillator (LO) combining capability using the two isolated gates as LO and RF ports. DG-FET mixers also provide the possibility of conversion gain. In this way, the need for a bulky coupler and IF amplifier can be eliminated, resulting in a small die size. Monolithic DG-FET mixers have been successfully implemented up to W-band [7]. Decent IMD performances have also been achieved experimentally using monolithic microwave integrated circuit (MMIC) DG-FET mixers [8]–[10]. Measured OIP_3's (third-order intercept points referred to the output) ranging from 5 to 10 dBm were reported. However, no research has been reported on the comprehensive analysis of intermodulation characteristics of DG-FET mixers, probably due to the complexity of dual-gate devices. Accordingly, design methodology to optimize the circuit for linearity and/or conversion gain has not been available for DG-FET mixers.

In this study, a general intermodulation analysis method of a DG-FET mixer has been developed at low transistor levels. The analysis is based on a time-varying Volterra series method [6]. Since the method was developed at the individual transistor levels, it allows one to probe the internal nodes of DG-FETs to evaluate the nonlinear current components, and, thus, helps to physically understand IMD generation mechanisms inside the DG-FET mixers. It also provides a way of assessing the role of each nonlinear component on the generation of IMD products. To prove the validity and generality of the proposed analysis method, two types of DG-FET mixers composed of cascode-connected high electron-mobility transistors (HEMTs) were designed and fabricated at X- and Ka-bands. A hybrid-type X-band mixer has been implemented using commercially available HEMTs, and a monolithic Ka-band mixer has been realized using pseudomorphic high electron-mobility transistors (pHEMTs) fabricated in-house at Seoul National University, Seoul, Korea. Both mixers showed excellent agreement between measured and simulated IMD characteristics, validating the analysis method. IMD "sweet spots" predicted by the analysis have also been verified experimentally for both cases. The bias-optimized X-band DG-FET mixer showed intermodulation characteristics comparable to those of the resistive mixers ($\mathrm{OIP}_3 \sim 13.6$ dBm versus 15.3 dBm for resistive mixers) with low LO power requirement.

Manuscript received June 20, 2000; revised May 15, 2001. This work was supported by the Korean Ministry of Science and Technology under the Creative Research Initiative Program.

The authors are with the Center for 3-D Millimeter-Wave Integrated Systems, School of Electrical Engineering, Seoul National University, Seoul 151-742, Korea.

Publisher Item Identifier S 0018-9480(02)05202-X.

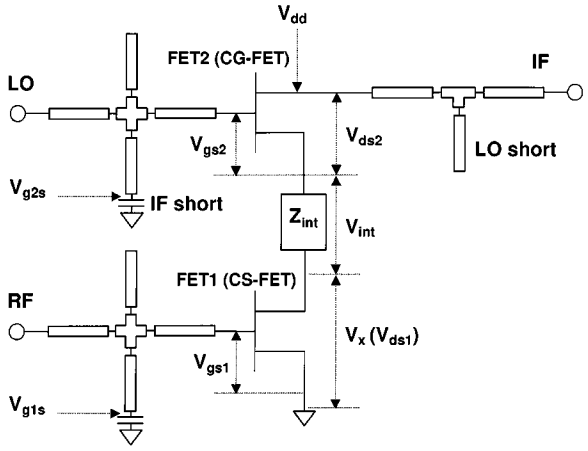

Fig. 1. Equivalent circuit schematic of a DG-FET mixer.

This paper provides a detailed IMD analysis and design methodology of DG-FET mixers for high linearity. It also shows that well-designed DG-FET mixers are very promising for modern monolithic applications requiring high linearity.

II. Intermodulation Analysis Method

The goal of this study was to understand the intermodulation mechanisms in DG-FET mixers and to identify the dominant sources of intermodulation and, finally, based on such information, to come up with a design method to optimize DG-FET mixers for high linearity. For this purpose, a custom computer program to analyze the IMD in DG-FET mixers has been developed on the basis of a time-varying Volterra-series method [11]. To simplify the analysis, a DG-FET was replaced by a cascode connection of two single-gate FETs so that the intermodulation analysis could be performed at single transistor levels rather than multitransistor ones. Fig. 1 shows the equivalent circuit schematic of a DG-FET mixer as represented by the cascode connection. Also shown in Fig. 1 is the circuit topology of the DG-FET mixer designed in this study, the details of which will be presented in Section V. As will be shown later, mixing mostly occurs in the lower CS-FET, which operates much like a drain-pumped mixer. The upper CG-FET provides LO pumping to the lower FET by changing the intermediate drain voltage (V_x in Fig. 1) in response to the LO signal. Nevertheless, the upper FET, which also works as a common-gate IF post-amplifier and mixer, may contribute to the overall IMD, as will be shown in Section IV.

A. Intermodulation Analysis Procedure

The analysis started by calculating the intermodulation products in the CS-FET, and is followed by a similar calculation in the CG-FET with different termination impedances and input signals. Thus, the nonlinear effects of the upper CG-FET were fully included in our analysis to generalize the analysis, as well as to quantify the contribution of the CG-FET on IMD generation.

Each calculation at the single-transistor levels was performed using an FET IMD analysis method presented in [6]. The method is based on a large-signal/small-signal analysis using a method of nonlinear currents, and was developed in [6] to analyze the single-gate mixers using CS-FETs. In this paper, the method has been extended and generalized so that it can be applied to the upper common-gate FET (CG-FET) as well.

The flowchart of the analysis program is shown in Fig. 2. The LO voltage waveform at each CS- and CG-FET was first evaluated by a single-tone harmonic-balance simulation using the LO signal as the only input. A commercial harmonic-balance simulator was used for this purpose. Once the LO waveform was found, perturbed small-signal current components were expressed in Taylor's series up to third order as follows:

$$i_d(v_g, v_d) = G_m v_g + G_d v_d + G_{m2} v_g^2 + G_{d2} v_d^2 + G_{md} v_g v_d + G_{m3} v_g^3 + G_{d3} v_d^3 + G_{m2d} v_g^2 v_d + G_{md2} v_g v_d^2 \quad (1)$$

where i_d is the drain current, v_g and v_d are the gate and drain voltage, respectively, and

$$G_{midj} = \frac{1}{(\max\{i,j\})!} \frac{\partial^{(i+j)} i_d}{\partial v_g^i \partial v_d^j} \quad (2)$$

where

$$\max\{i,j\} \equiv \begin{cases} i, & \text{if } i \geq j \\ j, & \text{otherwise.} \end{cases}$$

In (2), subscripts with zeroes and ones were omitted to simplify the notation, e.g., G_m denotes G_{m1d0} and G_{md} represents G_{m1d1}.

Fast Fourier transform (FFT) was followed to find harmonic frequency components of G_{midj}. Ten harmonics were included in the analysis. A set of Kirchoff's voltage law (KVL) equations was then derived at each mixing frequency using the small-signal equivalent circuit, and was solved by the method of nonlinear currents. The detail of the KVL equations and solution procedures will be presented in the following sections. After tedious, but straightforward calculations, each component of the third-order intermodulation currents shown in (1) was evaluated at the internal node (V_x in Fig. 1).

Among various IMD products generated by the CS-FET at IF and RF bands, only those with mathematical significance were selected and employed as the inputs to the lower CG-FET. The detailed selection criteria are given in Section IV. The IMD calculation procedure was then repeated for an upper CG-FET using different equations and input signals. Finally, the IMD products at the drain terminal of the cascode-connected FETs were found. The entire procedure was implemented in a computer program to speed up the simulation. The custom program allows one to probe any internal nodes to evaluate the nonlinear current components and, thus, helps to understand the mixing and intermodulation mechanisms inside the device.

B. Device Models

The analysis requires accurate knowledge of the voltage dependence of $G_m, G_{\rm ds}$ and their derivatives $(G_{midj}(v_{\rm gs}(t), v_{\rm ds}(t))$, which were provided by the voltage dependence tables of G_m and $G_{\rm ds}$. It also requires accurate estimation of the single-tone instantaneous LO voltage waveform

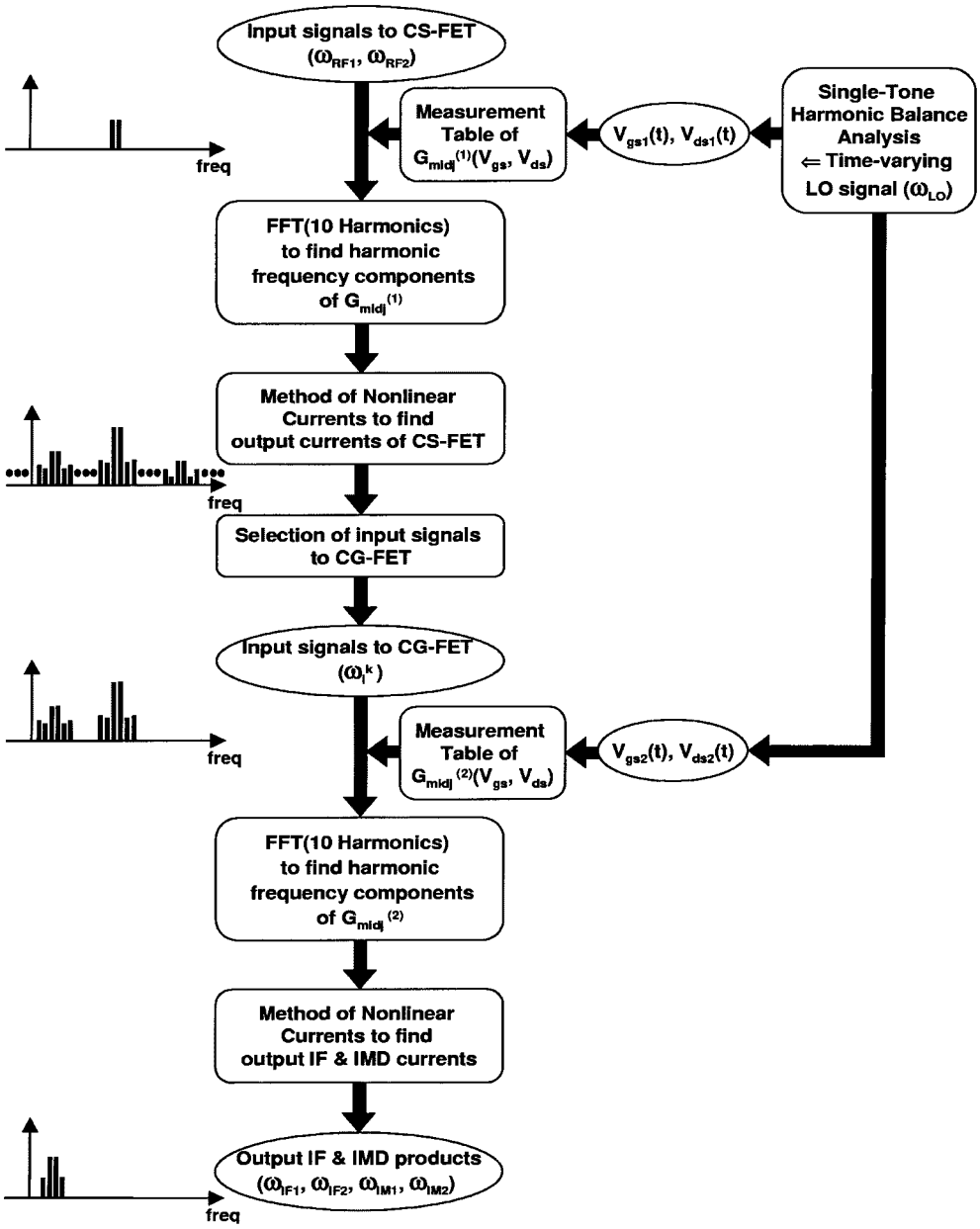

Fig. 2. Flowchart of the IMD analysis program of DG-FET mixers.

$(v_{\rm gs}(t), v_{\rm ds}(t))$ at each terminal of the FETs, which requires good nonlinear FET models.

The complete equivalent circuit of the DG-FETs used in this study is shown in Fig. 3. It includes nonlinear components as represented by two current sources and linear capacitive components, as well as parasitic elements such as access resistances and stray capacitances. Also included in this figure is the internal impedance labeled as "$Z_{\rm int}$," which represents connecting transmission lines between the two transistors, if any, and also the interstage matching circuits in cascode mixers, which may be included to improve performance.

The basic assumptions for the analysis are as follows. First, the capacitive effects due to nonlinear gate–source $(C_{\rm gs})$ and gate–drain $(C_{\rm gd})$ capacitances were neglected since they were far less significant than the nonlinear conductance effects due to G_m and $G_{\rm ds}$. Thus, they were considered as linear elements. Similar assumptions have been made for the analysis of single-gate FET mixers in [6]. Second, the reflections from the CG-FET was neglected to simplify the analysis. In this

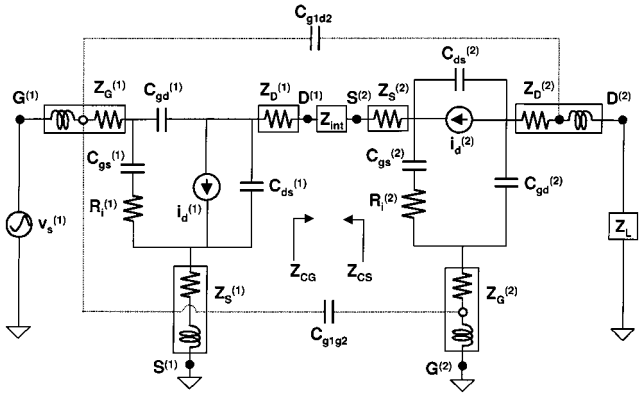

Fig. 3. Complete equivalent circuit of the DG-FETs used in this study.

way, multiple reflections between the CS- and CG-FETs could be ignored. Third, the effects of parasitic capacitances such as C_{g1d2} and C_{g1g2} were not included in the analysis.

The voltage dependence tables of G_{midj} have been extracted from the S-parameter measurements at various bias points. To improve the accuracy of the table, S-parameters were measured at fine steps ($\Delta V_g = 0.02$ V, $\Delta V_d = 0.02$ V) over the entire operation bias range of the DG-FET mixers. G_m and $G_{\rm ds}$ values were extracted using the small-signal extraction program developed in-house. The accuracy of the extraction program has been verified through successful demonstration of MMICs up to D-band [12], [13].

For the evaluation of large-signal LO voltage waveform, a modified table-based model presented in [14] has been used together with a commercial harmonic-balance simulator. Conventional table-based models are directly constructed from the measured data by numerical interpolation and integration. However, they may give erroneous results and cause ambiguity in *I–V* characteristics in the low drain voltage region due to the fact that the extracted conductance data may not satisfy numerical conservation condition. This may cause significant errors for simulations performed near the knee voltages, which is the case for the lower CS-FET of this study.

To improve the accuracy, a modified table-based model that combines the advantages of table-based and analytical models has been developed by Kwon *et al.* in [14]. Over the bias ranges where conservation condition is acceptably satisfied, the microwave current is calculated by integration using (3). On the other hand, for the bias regions where the current calculated by integration is questionable, the current is determined simply from the analytical I–V formula using the $\tanh$ function as follows:

$$I_{\rm ds}(V_{\rm gs}, V_{\rm ds}) = \int_0^{V_{\rm ds}} G_{22}(V_{\rm th}, \zeta)\, d\zeta + \int_0^{V_{\rm gs}} G_{21}(\zeta, V_{\rm ds})\, d\zeta \tag{3}$$

$$I_{\rm ds}(V_{\rm gs}, V_{\rm ds}) = (a + bV_{\rm ds}) \tanh(cV_{\rm ds}). \tag{4}$$

Finally, to satisfy the necessary continuity conditions, analytical formulas shown in (5)–(9) [15] are employed to fit the current and charge data calculated either from the integration or analytical methods as follows:

$$I_{\rm ds}(V_{\rm gs}, V_{\rm ds}) = (1/I_{\rm max} + 1/I_{\rm ds0})^{-1}. \tag{5}$$

The two individual current terms are

$$I_{\rm max}(V_{\rm ds}) = I_{\rm PK} \cdot \tanh(V_{\rm ds}/V_K)(1 + \lambda V_{\rm ds}) \tag{6}$$

$$I_{\rm ds0} = \exp\left(\psi(V_{\rm gs}, V_{\rm ds})\right) \tag{7}$$

where

$$\psi(V_{\rm gs}, V_{\rm ds}) = \sum_{i=0}^{m} a_i V_{\rm gs}^i \tag{8}$$

$$a_i(V_{\rm ds}) = \sum_{j=0}^{n} a_{ij} V_{\rm ds}^i. \tag{9}$$

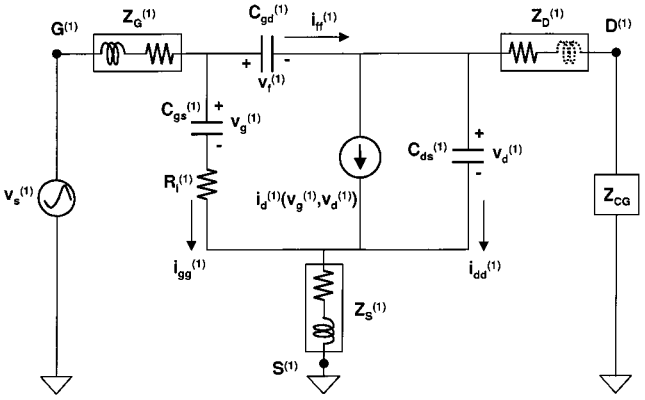

Fig. 4. Equivalent-circuit schematic of the lower CS-FET used for IMD analysis.

$I_{\rm PK}, V_K$, and a_{ij} are parameters that are determined by fitting to the microwave current data with weighting factors.

The model is numerically stable and produces accurate results. The model has been verified in [14] for millimeter-wave power amplifiers. In this study, the model has been refined, making use of the fact that the bias region required for mixer operation is limited compared to general circuits such as power amplifiers. For example, the lower CS-FET in DG-FET operates near the knee region only; the LO swing typically modulates the drain voltage from 0 V only up to 1.5–2 V. Hence, the model was primarily constructed based on the data measured densely in the knee region. The model was, in this way, capable of reproducing the conductances and their derivatives in the bias region of interest with high accuracy, as well as the current data themselves. The following two sections present detailed intermodulation analysis and results in the lower CS- and upper CG-FETs.

III. Intermodulation in the Lower CS-FET

The lower CS-FET operates like a drain-pumped mixer, where the LO signal modulates the drain voltage (V_x in Fig. 1). Subsequent variation of the transconductance and output conductance results in mixing operation. The RF signal is applied to the gate terminal and, thus, transconductance modulation with the LO signal is most responsible for mixing. As will be shown later, the nonlinear action of the CS-FET is not only responsible for mixing, but is also the largest source of IMD. A detailed intermodulation study has, consequently, been performed on the nonlinear effects of the CS-FET. In order to understand IMD mechanisms and to identify the major contributors to IMD inside the lower FET, the analysis began by investigating the intermodulation coefficients and proceeded to calculating each nonlinear current component of (1) and, finally, expressing them as phasors.

The equivalent circuit shown in Fig. 4 has been used to derive perturbed nonlinear current equations for the CS-FET. Frequency-dependent termination impedances ($Z_G, Z_S, Z_D, Z_{\rm CG}$) were employed to represent the impedances at each terminal of the CS-FET. $Z_{\rm CG}$ represents the input impedance of the CG-FET seen at the drain port of the CS-FET and may include $Z_{\rm int}$ if it exists for the case of cascode mixers. Using

KVL, the small-signal incremental current loop equations can be written in the following matrix forms [6]:

$$Z^{(1)}I^{(1)} = V^{(1)} \tag{10}$$

where superscript (1) denotes the CS-FET. Impedance matrix $Z^{(1)}$, current vector $I^{(1)}$, and voltage vector $V^{(1)}$ are as shown in (11)–(14), at the bottom of this page, where small-signal incremental currents $i_{\rm gg}^{(1)}, i_{\rm ff}^{(1)}$, and $i_{\rm dd}^{(1)}$, and small-signal incremental voltages $v_g^{(1)}, v_f^{(1)}$, and $v_d^{(1)}$ are specified in Fig. 4. $V_s^{(1)}$ is the voltage source that is determined according to the orders during the method of nonlinear currents.

Once the Taylor's expansion of all the small-signal drain current of (1) is substituted in (10), and all the time-varying functions are expanded in the frequency domain, the node voltage vector $V_n^{(1)}$ can be expressed as

$$V_n^{(1)} = \left[Z^{(1)}Y^{(1)} + 1\right]^{-1} V_s^{(1)} \tag{15}$$

where the admittance matrix $Y^{(1)}$ takes the form of a conversion matrix in mixers, and includes the nonlinear submatrices $G_m^{(1)}$ and $G_{\rm ds}^{(1)}$, as well as the linear submatrices $C_{\rm gs}^{(1)}, C_{\rm gd}^{(1)}$, and $C_{\rm ds}^{(1)}$ as

$$Y^{(1)} = \begin{pmatrix} j\Omega C_{\rm gs}^{(1)} & 0 & 0 \\ 0 & j\Omega C_{\rm gd}^{(1)} & 0 \\ G_m^{(1)} & 0 & G_{\rm ds}^{(1)} + j\Omega C_{\rm ds}^{(1)} \end{pmatrix} \tag{16}$$

where Ω is a diagonal submatrix whose diagonal elements correspond to the harmonic frequencies.

The method of nonlinear currents [11] is then applied to find the first-, second-, and third-order nonlinear currents. For the first-order calculations, the voltage source vector is

$$V_s^{(1)} = \begin{pmatrix} v_s^{(1)} \\ v_s^{(1)} \\ 0 \end{pmatrix}. \tag{17}$$

As soon as the first-order voltages are determined, the first-order output currents and the second-order current sources can be determined. This second-order current sources can then be transformed to the second-order voltage sources to solve the second-order equation. The calculation is repeated until the third-order nonlinear currents are found. Detailed simulation results are presented in the following sections.

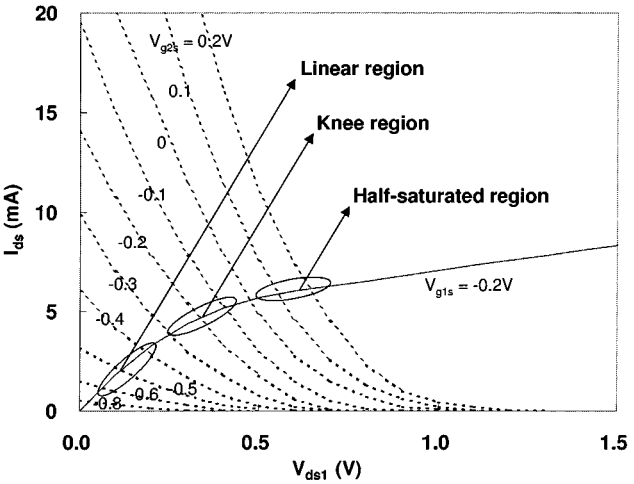

Fig. 5. *I–V* characteristic of a DG-FET at a fixed V_{g1s} of -0.2 V. According to V_{g2s}, three different bias regions of interest can be found and are denoted by circles.

A. Intermodulation Coefficients

As can be seen from (1), the third-order intermodulation products are most affected by the coefficients G_{m3}, G_{d3}, G_{md2}, and G_{m2d}. Accordingly, intermodulation can be minimized by studying these coefficients and selecting the bias and LO pumping conditions that minimize these coefficients. Similar studies have been performed for resistive mixers in [16] and [17], where Taylor-series coefficients of the I–V formula were related to IMD characteristics, and used to optimize the linearity of the resistive mixers.

Two independent gate biases determine the operating point of the DG-FETs. The gate bias to the lower FET (V_{g1s} in Fig. 1) determines the tradeoff between the conversion gain and noise figure, as shown in [18]. However, it has little effect on the linearity as long as the device is biased above pinchoff. The gate bias to the upper FET (V_{g2s} in Fig. 1), on the other hand, determines the operating point on the $I_{\rm ds}$–$V_{\rm ds}$ curve of the lower FET, as illustrated in Fig. 5. Since it determines the operating region of the CS-FET, it is expected to have strong effects on the coefficients. Fig. 6(a) and (b) shows measured transconductance,

$$Z^{(1)} = \begin{pmatrix} Z_G^{(1)} + R_i^{(1)} + Z_S^{(1)} & Z_D^{(1)} + Z_{\rm CG} & Z_S^{(1)} \\ Z_G^{(1)} & Z_G^{(1)} + Z_D^{(1)} + Z_{\rm CG} & -Z_D^{(1)} + Z_{\rm CG} \\ Z_S^{(1)} & -Z_D^{(1)} + Z_{\rm CG} & Z_D^{(1)} + Z_{\rm CG} + Z_S^{(1)} \end{pmatrix} \tag{11}$$

$$V^{(1)} = V_s^{(1)} - V_n^{(1)} \tag{12}$$

$$V_n^{(1)} = \begin{pmatrix} v_g^{(1)} \\ v_f^{(1)} \\ v_d^{(1)} \end{pmatrix} \tag{13}$$

$$I^{(1)} = \begin{pmatrix} i_{\rm gg}^{(1)} \\ i_{\rm ff}^{(1)} \\ i_{\rm dd}^{(1)} \end{pmatrix} \tag{14}$$

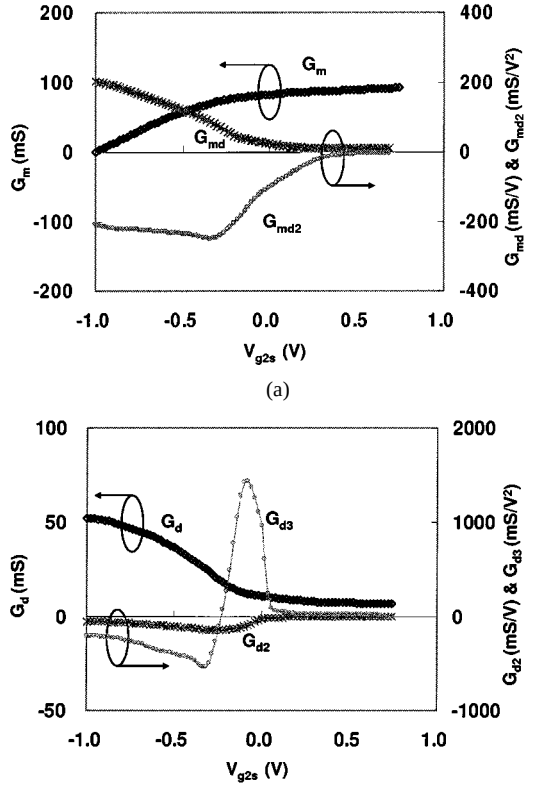

Fig. 6. Measured: (a) G_m, G_{md}, and G_{md2} and (b) G_d, G_{d2}, and G_{d3} coefficients of the 80-μm HEMT as a function of V_{g2s}.

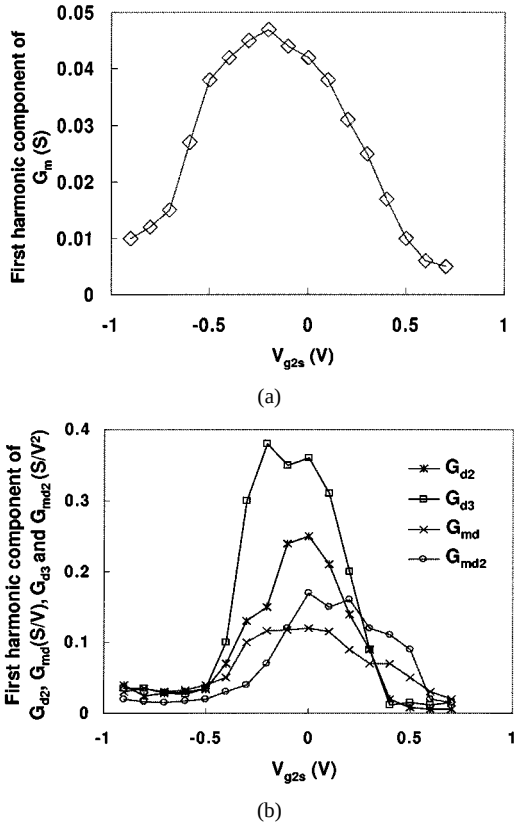

Fig. 7. First harmonic components of: (a) G_m and (b) G_{d2}, G_{md}, G_{d3}, and G_{md2} as a function of V_{g2s} at a fixed LO power of 0 dBm.

output conductance, and their derivatives, as a function of the second gate bias (V_{g2s}) for a fixed V_{g1s} of -0.2 V. $V_{\rm dd}$ was set to 3 V for this measurement. The conversion gain of the mixer largely depends on the variation of transconductance with LO pumping. To be more specific, the fundamental harmonic component of $G_m(V_{g2s}(t))$ under LO pumping determines conversion gain [12]. Fig. 6(a) shows that the highest conversion gain is expected near the knee voltage ($V_{g2s} \sim -0.2$ V: "knee region" in Fig. 5), where G_m curve shows the greatest change. However, poor intermodulation characteristics are also expected in this bias region, as shown in Fig. 6(b). Fig. 6(b) shows that G_{d3}, which will be shown to have the greatest impact on $\rm IMD_3$ generation later, presents the largest value and change near the knee voltage ($V_{g2s} \sim -0.2$ V). This means that poor intermodulation performance is unavoidable when the DG-FET mixer is bias tuned for maximum conversion gain. In order to clarify this point, the first harmonic components of the intermodulation coefficients of (2) are calculated and plotted in Fig. 7 as a function of V_{g2s}. For this calculation, the LO voltage waveform was found from the harmonic-balance simulation, and a subsequent FFT was performed using the time-domain conductance data. As expected, the first harmonic components of G_m and G_{d3} coefficients show peak values near the knee voltage. It is also worthwhile to note that the G_m peak is broader than the G_{d3} peak. The rapid decrease of the G_{d3} coefficient outside the knee region suggests that excellent intermodulation characteristics can be achieved together with decent conversion gain by choosing the V_{g2s} just outside of the knee region (V_{g2s} near -0.5 V: "linear region" and 0.2 V: "half-saturated region" in Fig. 5). This point will be verified by further simulation and measurement.

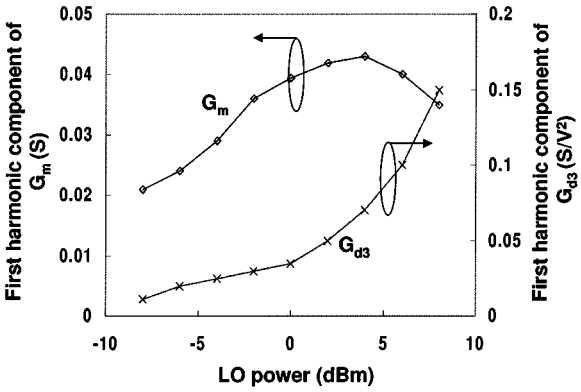

Fig. 8. First harmonic components of G_m and G_{d3} as a function of LO power. V_{g2s} was fixed at -0.5 V.

Besides the gate bias, the LO pumping level also has a strong effect on the conversion gain and linearity. Fig. 8 shows the first harmonic components of G_m and G_{d3} as a function of LO power. The rapid increase of the G_{d3} coefficient at high LO power levels implies that the LO pumping level must be maintained below a certain level (4 dBm) to achieve good linearity. The decrease of the G_m component at high LO power levels also suggests that optimum LO power be around 0–3 dBm.

B. Phasor Diagram Analysis and Simulation Results

The third-order intermodulation current is composed of various components, as shown in (1). Each term in (1) is a vector

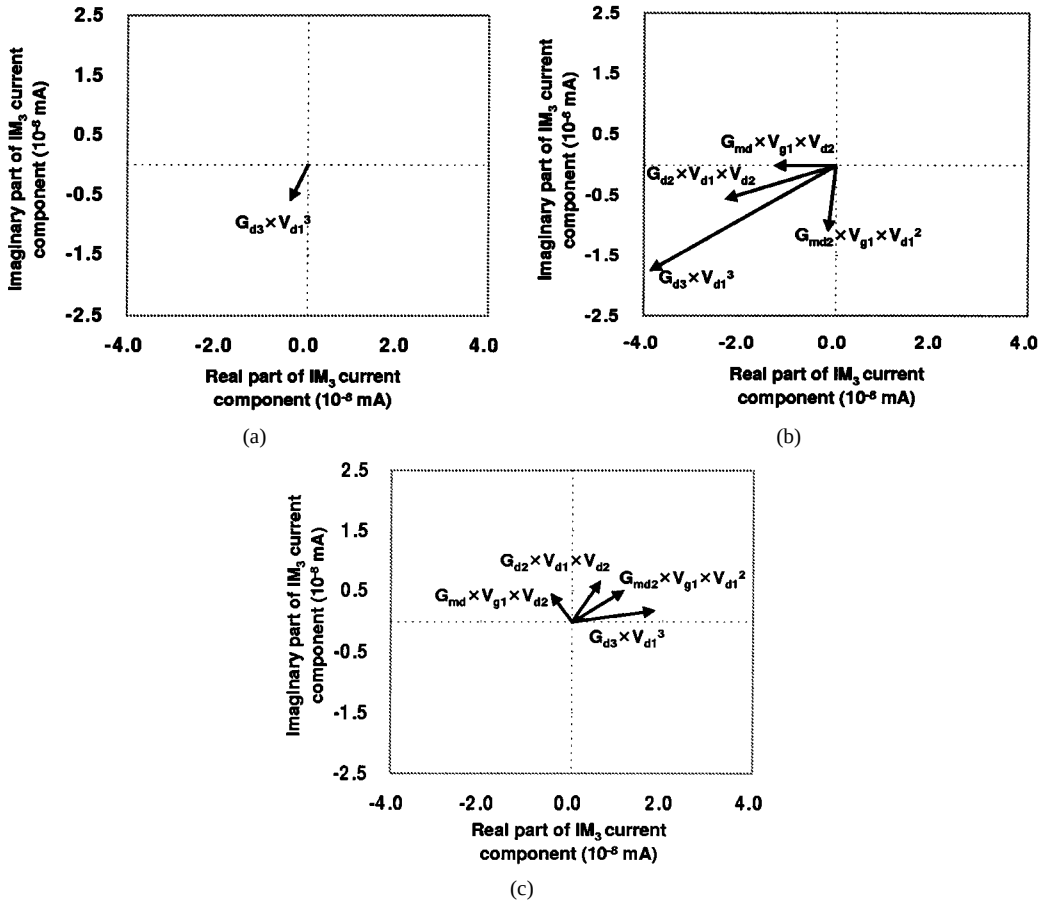

Fig. 9. Phasor diagrams comparing nonlinear current components, corresponding to: (a) linear region, (b) knee region, and (c) half-saturated region.

quantity with both magnitude and phase. Thus, it can be represented as a complex phasor, as in [19], and the total intermodulation current as a vector sum of each component. In order to identify dominant terms generating IMD, terms of (1) are expressed with the help of phasors in the two-dimensional (2-D) complex plane, as shown in Fig. 9. In the previous section, the intermodulation coefficients were shown to be strongly dependent on the second gate bias. Similar characteristics are expected for the intermodulation current terms. Thus, Fig. 9 shows three different phasor diagrams corresponding to the following bias regions:

1) linear region;
2) knee region;
3) half-saturated region;

according to the notations in Fig. 5. The LO power is fixed at 0 dBm for this calculation, corresponding to the optimum pumping level judged from Fig. 8.

Even though the phase and magnitude of intermodulation phasors vary according to bias, it can be generally stated from Fig. 9 that the nonlinearities related to the output conductance (G_{d2} and G_{d3}) dominate the overall intermodulation in most bias regions. The largest intermodulation occurs in the knee region [see Fig. 9(b)]. In this region, the two output conductance nonlinearities G_{d2} and G_{d3} add nearly in-phase, producing the largest intermodulation products. Terms due to G_d nonlinearities decreases rapidly as the bias is shifted away from the knee region. Minimum intermodulation is observed in the linear region [see Fig. 9(a)], which shows greatly reduced G_d terms and almost negligible transconductance terms. The relative importance of transconductance nonlinearities (G_{md} and G_{md2}) grows as the bias moves toward saturation. In the half-saturated region [see Fig. 9(c)], the G_{md} and G_{md2} current terms contribute to about 40% of the total IMD. However, the overall intermodulation in this region still remains much smaller than that in the knee region. On the whole, the dominant intermodulation sources are G_d-related terms, and the intermodulation can be greatly reduced by selecting V_{g2s}, which minimize G_d terms.

IV. Intermodulation in the Upper CG-FET

The upper FET operates much like a source follower. It provides the LO signal to the lower CS-FET. The main action taking place in the CG-FET was considered by many designers as mere IF post-amplification. Mixing in a CG-FET was thought to be negligible. Furthermore, its role for IMD generation has not been well understood. In order to accurately assess the role of the CG-FET in mixing and intermodulation generation, a full intermodulation analysis similar to the case of the CS-FET described in the previous section was performed on the upper FET. The equivalent-circuit schematic shown in Fig. 10 has been employed to derive perturbed nonlinear current equations for the CG-FET. A set of equations similar to those derived for the CS-FET [see (11)–(16)] has been derived for the CG-FET. Here, superscript (2) represents the CG-FET as follows:

$$V_n^{(2)} = \left[Z^{(2)}Y^{(2)} + 1\right]^{-1}\left(-V_s^{(2)}\right) \tag{18}$$

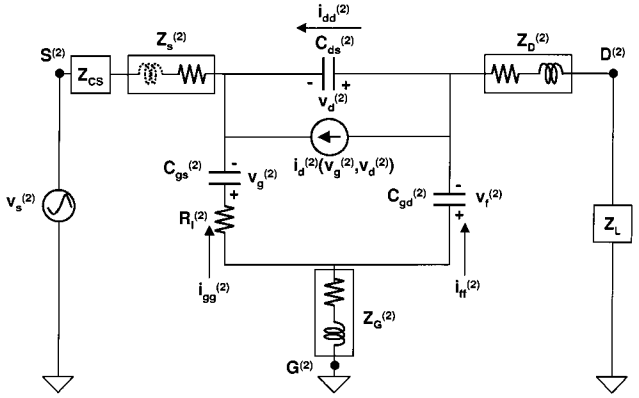

Fig. 10. Equivalent-circuit schematic of the upper CG-FET used for IMD analysis.

and as $Z^{(2)}$ and $Y^{(2)}$, shown in (19) and (20), at the bottom of this page, where $Z_{\rm CS}$ represents the output impedance of the CS-FET seen at the source terminal of the CG-FET, and may also include $Z_{\rm int}$ for cascode mixers. Overall matrix elements and calculation procedures are very similar to the case of the CS-FET, except for the termination impedances and input voltage source vectors. For example, the following first-order voltage source vector is used for CG-FET calculation:

$$V_s^{(2)} = \begin{pmatrix} v_s^{(2)} \\ 0 \\ v_s^{(2)} \end{pmatrix}. \tag{21}$$

It is worthwhile to note that the first-order sources, or the input signals to the CG-FET, are much more complicated than those of CS-FETs since, in principle, they should comprise all the output components from the CS-FET. However, this makes analytical derivation practically impossible. Thus, a selection procedure is needed at this stage. Selection was made to include all the dominant frequency components that will eventually appear at the IF load via mixing or amplification in the CG-FET. Eighteen components ($\omega_i^k = k\omega_{\rm LO} + \omega_i (i = 1, 2, 3, \ldots, 9, k = 0, 1)$) have been selected as the inputs to the CG-FET; 9 components ($\omega_i (i = 1, 2, 3, \ldots, 9)$) each with orders less than or equal to three have been chosen from IF ($k = 0$) and RF ($k = 1$) bands. The spectrum of the 18 input frequency components is shown in Fig. 11 together with the voltage magnitudes of each component in a separate table. The largest terms are the RF components at $\omega_{\rm RF1}$ ($=\omega_1^1$) and $\omega_{\rm RF2}$ ($=\omega_2^1$), followed by the downconverted IF components at $\omega_{\rm IF1}$ ($=\omega_1^0$) and $\omega_{\rm IF2}$ ($=\omega_2^0$). It is worthwhile to note that the components at the RF band ($k = 1$ or $\omega_{\rm LO} + \omega_i$) are greater by a factor of two to three than the corresponding components at the IF band ($k = 0$ or ω_i). This can

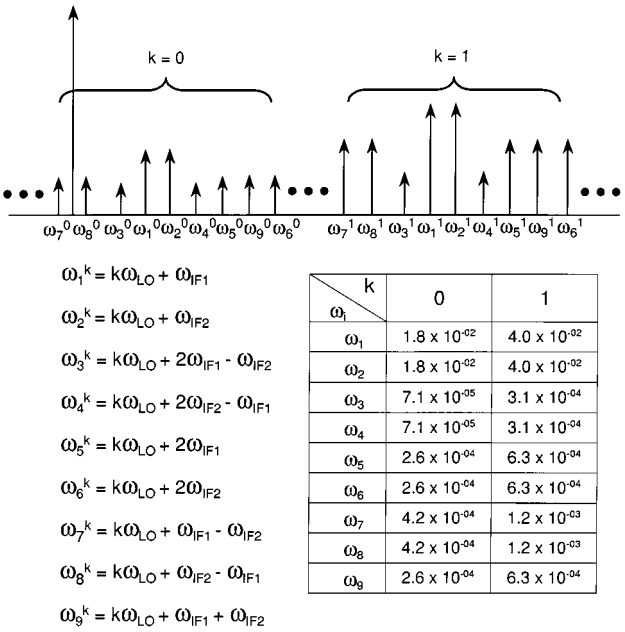

ω_i \ k	0	1
ω_1	1.8 x 10^{-02}	4.0 x 10^{-02}
ω_2	1.8 x 10^{-02}	4.0 x 10^{-02}
ω_3	7.1 x 10^{-05}	3.1 x 10^{-04}
ω_4	7.1 x 10^{-05}	3.1 x 10^{-04}
ω_5	2.6 x 10^{-04}	6.3 x 10^{-04}
ω_6	2.6 x 10^{-04}	6.3 x 10^{-04}
ω_7	4.2 x 10^{-04}	1.2 x 10^{-03}
ω_8	4.2 x 10^{-04}	1.2 x 10^{-03}
ω_9	2.6 x 10^{-04}	6.3 x 10^{-04}

Fig. 11. Spectrum of the 18 frequency components selected as the inputs to the upper CG-FET for IMD simulation. Shown in the separate table are the voltage amplitudes (V) of each frequency component.

be easily understood if one considers that the IF components are downconverted signals from their RF counterparts.

Given the inputs shown in Fig. 11, the following four frequency components of interest have been calculated at the load: $\omega_{\rm IF1}, \omega_{\rm IF2}, \omega_{\rm IM1}$ ($=2\omega_{\rm IF1} - \omega_{\rm IF2}$), $\omega_{\rm IM2}$ ($=2\omega_{\rm IF2} - \omega_{\rm IF1}$). In order to identify the major sources of intermodulation, each frequency component has been sorted according to the frequency and the order of mixing. For example, the IF intermodulation product at $2\omega_{\rm IF1} - \omega_{\rm IF2}$ (IM1) was sorted as follows:

$$I_{\rm IM1} = I_{\rm IFlin} + I_{\rm RFmix1} + I_{\rm RFmix2} + I_{\rm IFim} + \text{higher order terms} \tag{22}$$

where

$$I_{\rm IFlin} = G_{m1}^{(0)} V_{2\omega_{\rm IF1} - \omega_{\rm IF2}} \tag{23}$$

$$I_{\rm RFmix1} = G_{m1}^{(1)} V_{2\omega_{\rm RF1} - \omega_{\rm RF2}} \tag{24}$$

$$I_{\rm RFmix2} = \left\{ 2G_{m2}^{(1)} \left(V_{\omega_{\rm RF1} - \omega_{\rm RF2}} V_{\omega_{\rm RF1}} + V_{2\omega_{\rm RF1}} V_{\omega_{-\rm RF2}} \right) + 3G_{m3}^{(1)} V_{\omega_{\rm RF1}} V_{\omega_{\rm RF1}} V_{\omega_{-\rm RF2}} \right\} \tag{25}$$

$$I_{\rm IFim} = \left\{ 2G_{m2}^{(0)} \left(V_{\omega_{\rm IF1} - \omega_{\rm IF2}} V_{\omega_{\rm IF1}} + V_{2\omega_{\rm IF1}} V_{\omega_{-\rm IF2}} \right) + 3G_{m3}^{(0)} V_{\omega_{\rm IF1}} V_{\omega_{\rm IF1}} V_{\omega_{-\rm IF2}} \right\} \tag{26}$$

and $G^{(k)}$ represents the kth harmonic component of G.

$$Z^{(2)} = \begin{pmatrix} Z_G^{(2)} + R_i^{(2)} + Z_S^{(2)} + Z_{\rm CS} & Z_D^{(2)} + Z_L & Z_S^{(2)} + Z_{\rm CS} \\ Z_G^{(2)} & Z_G^{(2)} + Z_D^{(2)} + Z_L & -Z_D^{(2)} + Z_L \\ Z_S^{(2)} + Z_{\rm CS} & -Z_D^{(2)} + Z_L & Z_D^{(2)} + Z_L + Z_S^{(2)} + Z_{\rm CS} \end{pmatrix} \tag{19}$$

$$Y^{(2)} = \begin{pmatrix} j\Omega C_{\rm gs}^{(2)} & 0 & 0 \\ 0 & j\Omega C_{\rm gd}^{(2)} & 0 \\ G_m^{(2)} & 0 & G_{\rm ds}^{(2)} + j\Omega C_{\rm ds}^{(2)} \end{pmatrix} \tag{20}$$

TABLE I
AMPLITUDE AND PHASE OF SORTED CURRENT COMPONENTS ($I_{\mathrm{IFlin}}, I_{\mathrm{RFmix1}}, I_{\mathrm{RFmix2}}$ AND I_{IFim} OF (4)–(7)) CALCULATED AT VARIOUS LO PUMPING POWER LEVELS. MIXING COMPONENTS AT ω_{IF1} ARE LISTED IN (a), WHILE THE INTERMODULATION COMPONENTS AT ω_{IM1} $(=2\omega_{\mathrm{IF1}} - \omega_{\mathrm{IF2}})$ ARE SHOWN IN (b)

I_{IF1}	P_{LO}=−5 dBm	P_{LO}=0 dBm	P_{LO}=5 dBm	P_{LO}=10 dBm
I_{IFlin}	$7.9\times10^{-4}\angle-85°$	$1.1\times10^{-3}\angle-82°$	$1.4\times10^{-3}\angle-78°$	$1.3\times10^{-3}\angle-80°$
I_{RFmix1}	$2.2\times10^{-4}\angle-180°$	$5.6\times10^{-4}\angle-171°$	$8.0\times10^{-4}\angle-172°$	$1.1\times10^{-3}\angle-174°$
I_{RFmix2}	$2.2\times10^{-6}\angle-77°$	$3.6\times10^{-6}\angle-64°$	$1.4\times10^{-5}\angle-90°$	$2.4\times10^{-5}\angle-64°$
I_{IFim}	$1.1\times10^{-6}\angle-153°$	$1.4\times10^{-6}\angle-134°$	$6.8\times10^{-6}\angle-127°$	$1.5\times10^{-5}\angle-179°$

(a)

I_{IF1}	P_{LO}=−5 dBm	P_{LO}=0 dBm	P_{LO}=5 dBm	P_{LO}=10 dBm
I_{IFlin}	$4.5\times10^{-6}\angle-102°$	$5.6\times10^{-6}\angle-100°$	$1.8\times10^{-5}\angle-100°$	$2.5\times10^{-5}\angle-103°$
I_{RFmix1}	$1.1\times10^{-6}\angle-176°$	$1.4\times10^{-6}\angle-174°$	$4.5\times10^{-6}\angle-170°$	$6.3\times10^{-6}\angle-174°$
I_{RFmix2}	$2.5\times10^{-6}\angle-68°$	$4.1\times10^{-6}\angle-60°$	$1.0\times10^{-5}\angle-59°$	$2.0\times10^{-5}\angle-82°$
I_{IFim}	$1.2\times10^{-6}\angle-150°$	$1.2\times10^{-6}\angle-124°$	$6.2\times10^{-6}\angle-155°$	$1.0\times10^{-5}\angle-172°$

(b)

I_{IFlin} represents linear amplification terms that are essentially the intermodulation terms generated by the lower CS-FET and linearly amplified in the upper FET. I_{RFmix1} includes first-order mixing terms that have been frequency translated from $2\omega_{\mathrm{RF1}} - \omega_{\mathrm{RF2}}$ to $2\omega_{\mathrm{IF1}} - \omega_{\mathrm{IF2}}$. Thus, for this component, the intermodulation was generated in the CS-FET and downconverted to the IF band by mixing in the CG-FET. I_{RFmix2} represents the second- and third-order mixing terms resulting from intermixing of ω_{RF1} and $\omega_{\mathrm{RF1}} - \omega_{\mathrm{RF2}}, \omega_{\mathrm{RF1}}$ and ω_{RF2}, and so on. These terms were generated by intermodulation in the CG-FET and downconverted to the IF band by mixing in the same device. Lastly, I_{IFim} terms denote intermodulation products at IF frequencies. No frequency translation is involved in the CG-FET for this term. Thus, they represent intermodulation terms produced during post-amplification of IF-band signals in the CG-FET. The generation of I_{RFmix2} and I_{IFim} IMD terms is attributed exclusively to the nonlinear effects of the CG-FET. Similar categorization can be carried out on other IF frequency components. Table I shows each sorted current component calculated at four different LO pumping power levels. Mixing components at ω_{IF1} are listed in Table I(a), while the intermodulation components at $2\omega_{\mathrm{IF1}} - \omega_{\mathrm{IF2}}$ are shown in Table I(b). The following observations can be made from the simulation results of Table I.

1) Higher order intermixing in the CG-FET has a negligible effect on the mixing component (IF1); I_{IFim} and I_{RFmix2} terms are insignificant compared to I_{RFmix1} and I_{IFlin} [two orders of magnitude smaller, as shown in Table I(a)].
2) The downconverted IF1 component due to mixing in the CG-FET (I_{RFmix1}) is smaller than the linearly post-amplified term (I_{IFlin}) at low LO power levels. However, it grows with LO power and becomes nonnegligible at high LO power levels, implying that the mixing effect in the upper FET needs to be considered for conversion-loss calculation at high LO power levels.
3) Unlike the mixing component (IF1), a significant portion of the intermodulation term IM1 is generated by higher order intermixing in the CG-FET. As a matter of fact, the second– and third-order RF intermodulation term I_{RFmix2} is comparable to the linear term I_{IFlin} over the entire LO power range used in the simulation [see Table I(b)].
4) IMD during post-amplification of IF signals (I_{IFim}) also cannot be neglected. This, together with the importance of I_{RFmix2}, means that the CG-FET contributes significantly to the overall IMD and, consequently, the intermixing effect of the CG-FET has to be included for accurate estimation of IMD in DG-FET mixers.

Following the above observations, it can be stated that the upper CG-FET operates more than just a simple linear post IF amplifier. It does indeed complicate the picture by adding its own nonlinearities, especially at high LO power levels. To make matters worse, its effect is more pronounced in producing intermodulation products than mixing terms; major mixing action still takes place in the lower CS-FET, but the intermodulation products will grow measurably after the signal passes through the upper FET. Therefore, the nonlinear effects of the CG-FET have to be considered for accurate simulation of IMD, and special care has to be taken not to use excessive LO powers and to keep the CG-FET in the linear-operation region for high-linearity design.

In order to visualize the nonlinear effect of the CG-FET, the calculated IF power and the power level of the third-order intermodulation components are plotted in Fig. 12 as a function of the LO power for two signals: one before and the other after passing through the upper FET. The RF power was −20 dBm. The curves labeled as "IF-out" and "$\mathrm{IMD_3}$-out" denote the output signals after the CG-FET and those labeled as "IF-in" and "$\mathrm{IMD_3}$-in" are the input signals into the CG-FET. As expected earlier, IMD increases with the LO power. Rapid increase of intermodulation above 0 dBm in Fig. 12 again indicates that the optimum LO power is around 0 dBm. At this LO power level, the relative intermodulation power (referenced to the IF signal) increases from −48 dBc to −44 dBc after the signal passes through the CG-FET. This corresponds to a 2-dB decrease in the third-order intercept point $(\mathrm{OIP_3})$, which illustrates a nonnegligible impact of the CG-FET on linearity.

V. DESIGN AND RESULTS

To verify the analysis method and to demonstrate generality of the proposed analysis, two types of linearity-optimized DG-FET mixers composed of cascode-connected HEMTs

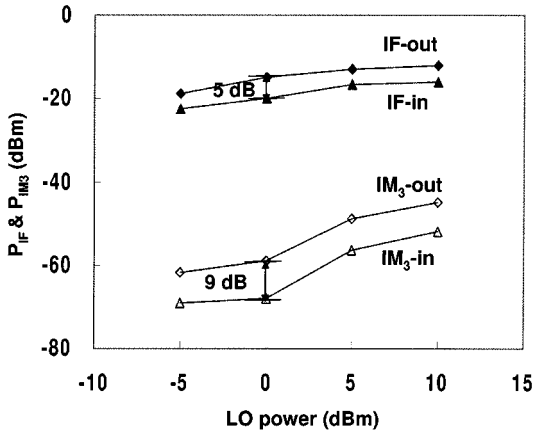

Fig. 12. Power of IF and third-order intermodulation signals as a function of the LO power. The curves labeled "-in" correspond to the signals before entering the CG-FET, and those labeled "-out" represent the signals after passing through the CG-FET.

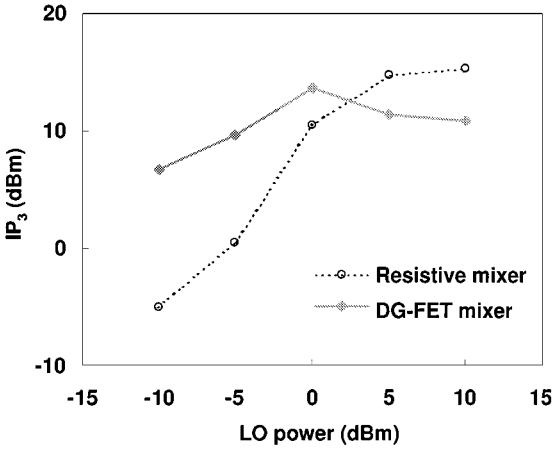

Fig. 14. Comparison of measured IP_3 between the resistive mixer and DG-FET mixer as a function of LO power. Both mixers used the same transistor, a commercial 80-μm HEMT.

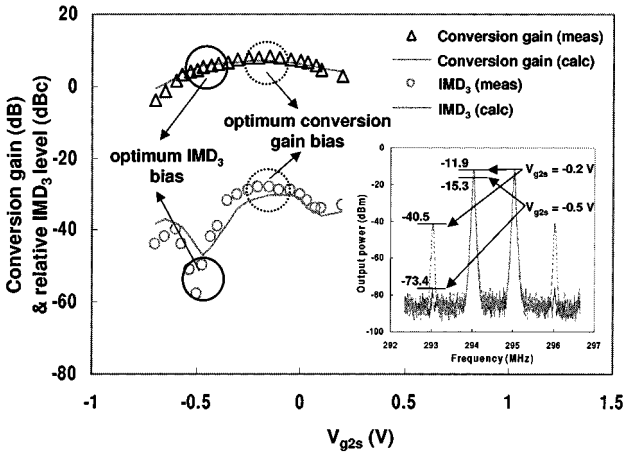

Fig. 13. Measured and calculated conversion gain and relative intermodulation level (IMD_3) of the X-band DG-FET mixer at a fixed V_{g1s} of -0.2 V and V_{dd} of 3 V. RF input power is -20 dBm and LO power is 0 dBm. Also shown in the inset are the spectrums of IF and IM_3 signals at two distinct bias points: $V_{g2s} = -0.2$ V (optimum conversion gain) and -0.5 V (optimum IMD_3).

were fabricated at two different frequencies using different types of transistors. First, commercially available HEMTs were used to realize a hybrid-type X-band mixer. Another mixer was fabricated at the Ka-band using 0.2-μm GaAs pHEMTs developed in-house. The Ka-band mixer is a monolithic circuit and the epitaxial layer structure is different from the X-band device, resulting in different nonlinear characteristics.

Fig. 1 shows the equivalent-circuit schematic of the X-band hybrid mixer. The gate bias network included a $\lambda/4$ transmission line terminated with a large capacitor for an IF short. An LO short was provided at the output using a radial stub. RF and LO matching circuits were realized with open-ended stubs. No IF matching was included in the circuit, making the IF load impedance 50 Ω. The frequencies of the two-tone RF signals were 10 and 10.001 GHz and the LO frequency was 9.7 GHz, resulting in IF two-tone signals at 300 and 301 MHz.

Fig. 13 shows the measured and calculated conversion gain and IMD_3 of the X-band mixer as a function of V_{g2s} at a fixed V_{g1s} of -0.2 V and V_{dd} of 3 V. RF input power was -20 dBm and LO power was 0 dBm. As expected earlier, maximum conversion gain was observed near the knee voltage ($V_{g2s} = -0.2$ V), corresponding to the peak point of the first harmonic component of G_m in Fig. 7(a). This bias point, however, showed the worst IMD characteristics with an IMD_3 of -28.6 dBc. As the bias is moved out of the knee region, IMD characteristics improved with a slight decrease in the conversion gain. Minimum IMD distortion was observed at a V_{g2s} of -0.5 V. This point was consistent with the intermodulation "sweet spot" predicted from the intermodulation coefficient analysis in Section III. Also shown in the inset are the spectrums of IF and IM signals at these two bias points. The measured IMD_3 level at $V_{g2s} = -0.5$ V was -58.1 dBc, which was as much as a 29.5-dB improvement over the value at the knee bias region ($V_{g2s} = -0.2$ V). The conversion gain decreased only by 3.4 dB from 8.1 to 4.7 dB. Fig. 13 shows an important characteristic of a DG-FET mixer that the circuit can be optimized either for conversion gain or linearity by simple tuning of V_{g2s} bias. Fig. 13 also shows excellent correspondence between the measurement and simulation for both conversion gain and IMD_3; measured conversion gain was within 1 dB of the simulation, and measured IMD_3 was within 5 dB for most bias conditions. Good agreement between measured and simulated data proves the validity of our analysis method.

To benchmark the linearity of the DG-FET mixer of this study, a resistive mixer was designed and fabricated using the same transistor at X-band. Measured OIP_3 is compared as a function of the LO power in Fig. 14. The resistive mixer showed a peak IP_3 of 15.3 dBm at a high LO power of 10 dBm. The DG-FET mixer showed a slightly lower peak IP_3 of 13.6 dBm, but at a much lower LO power of 0 dBm. This demonstrates that properly designed DG-FET mixer can show linearity characteristics not so much inferior to resistive mixers, but with lower LO power requirement, as well as favorable conversion gain and inherent RF/LO isolation capability.

To prove the general adequacy of the proposed intermodulation analysis, we also made two-tone measurements of a Ka-band HEMT MMIC mixer. Two transistors with a gate periphery of 80 μm have been used in a cascode configuration. The frequencies of the two-tone RF signals were 27 and

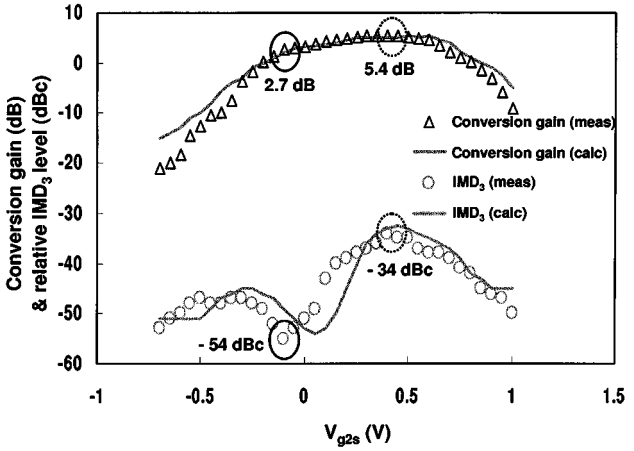

Fig. 15. Measured and calculated conversion gain and relative intermodulation level (IMD_3) of the Ka-band DG-FET mixer at a fixed V_{g1s} of -0.2 V and V_{dd} of 3 V. RF input power is -20 dBm and LO power is 0 dBm: $V_{g2s} = 0.4$ V corresponds to optimum conversion gain and -0.1 V to optimum IMD_3 bias points.

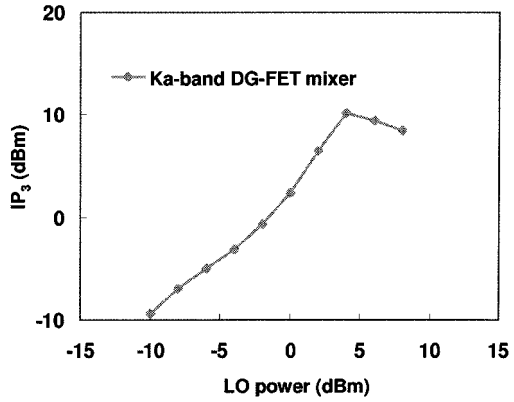

Fig. 16. Measured OIP_3 as a function of the LO power for the Ka-band mixer.

27.001 GHz and the LO frequency was 26.5 GHz, resulting in IF two-tone signals at 500 and 501 MHz.

The comparison of the measured and calculated conversion gain and IMD_3 as a function of V_{g2s} is shown in Fig. 15. As in the case of the X-band hybrid mixer, the intermodulation "sweet spot" was observed at a V_{g2s} of -0.1 V, showing 20-dBc improvement over the value at the knee bias region ($V_{g2s} = 0.4$ V). Good agreement between simulation and measurement again verifies the accuracy of the proposed analysis. Fig. 16 shows the measured OIP_3 as a function of the LO power. This proves that there is also an optimum LO power ($\sim$1 dBm) for IMD for the Ka-band DG-FET mixer.

Fig. 17 shows measured OIP_3 and conversion gain as a function of the drain bias (V_{dd}) for both mixers. Excellent IP_3 characteristics hold out to a very low drain bias of 0.8 V at X-band [see Fig. 17(a)]. High OIP_3's more than 13 dBm were found over a broad drain bias range from 0.8 to 3 V. At a drain bias of 2 V, an OIP_3 of 13.6 dBm was obtained together with a low dc power consumption of 6 mW. Similar characteristics have also been observed for the Ka-band monolithic mixer, as shown in Fig. 17(b). IP_3 higher than 10 dBm have been achieved down to a low drain bias of 1.2 V at Ka-band.

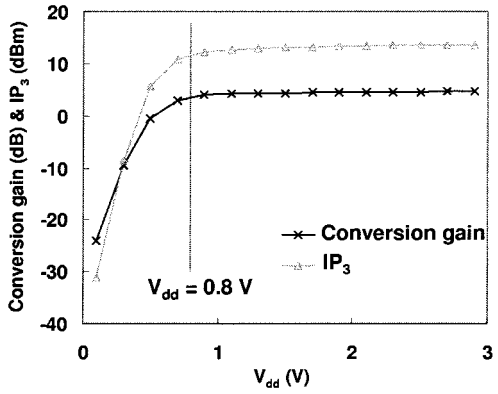

(a)

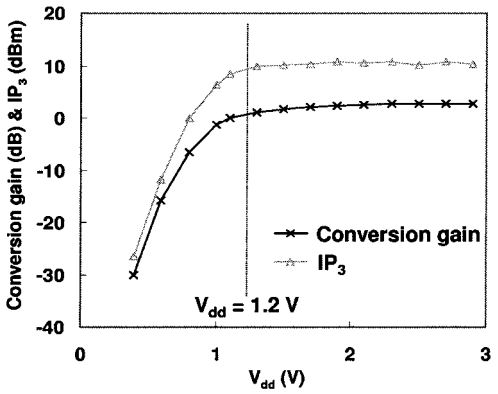

(b)

Fig. 17. Measured conversion gain and third-order output intercept points (IP_3): (a) of the X-band commercially available cascode mixer and (b) the Ka-band monolithic cascode mixer as a function of V_{dd}.

VI. Conclusion

A detailed intermodulation analysis program has been developed to simulate the IMD performance of DG-FET mixers. The program was based on a large-signal/small-signal analysis method, where a commercial harmonic-balance program was used to find large-signal LO waveforms, and Volterra series for perturbed small-signal analysis. For the analysis, the DG-FET was broken down into a cascode connection of a CS-FET and CG-FET. A comprehensive IMD study was carried out at the individual transistor levels to obtain physical understanding of intermodulation mechanisms inside the DG-FETs.

A quantitative IMD comparison study has shown that the contribution of the CS-FET on IMD generation was found to be predominant over that of the CG-FET. Yet it was also found that, at high LO power levels, nontrivial IMD can be added by the CG-FET due to its own nonlinearities. In other words, major mixing and IMD action takes place in CS-FET, but IMD can grow measurably after passing through the CG-FET depending on the LO power levels. Therefore, the nonlinear effects of the CG-FET should be included for accurate IMD simulation, and special care has to be taken not to use excessive LO powers for high linearity.

Since the CS-FET was found to be the largest source of IMD, a thorough intermodulation study has been performed to identify the major contributors to IMD inside the CS-FET. After investigating the intermodulation coefficients and comparing each

nonlinear current component with the help of phasors, it was revealed that the nonlinearities related to the output conductance dominate the overall IMD in the CS-FET. It was also found that G_d nonlinearities show strong dependence on the second gate bias (V_{g2s}). The largest intermodulation occurs in the knee region, where G_d nonlinearities add in-phase and produce large intermodulation products. However, G_d nonlinearities decrease rapidly as the bias is shifted away from the knee region. Minimum IMD is observed in the linear region right next to the knee bias. Respectable conversion gain is also observed in this region, suggesting that it correspond to a "sweet spot" for linearity. IMD dependence on LO power was also studied. The rapid increase of the G_{d3} coefficient at high LO power levels implies that the LO pumping level must be maintained below a certain level (4 dBm) to achieve good linearity.

Based on the analysis results, two types of illustrative DG-FET mixers, both optimized for linearity, have been designed and fabricated using different devices at X- and Ka-bands. Excellent IMD characteristics were achieved using a drain bias as low as 0.8 V at X-band and 1.2 V at Ka-band. Measured OIP_3 of an X-band DG-FET mixer (13.6 dBm) compares well with that of the resistive mixers (15.3 dBm) using the same FET. The presence of IMD "sweet spots" predicted by the analysis was also proven experimentally. Very good agreement between the measurement and simulation was found for both types of mixers, which validates our analysis method and supports the general adequacy of our approach. This paper has shown that well-designed DG-FET mixers are very promising for modern monolithic applications requiring high linearity. The analysis of this paper can be further used to optimize the linearity of DG-FET or cascode mixers.

ACKNOWLEDGMENT

The authors would like to thank M. S. Jeon, WavIC Inc., Seoul, Korea, for technical assistance during testing and measurement.

REFERENCES

[1] S. A. Maas, "Two-tone intermodulation in diode mixers," *IEEE Trans. Microwave Theory Tech.*, vol. MTT-35, pp. 307–315, Mar. 1987.

[2] R. S. Virk and S. A. Mass, "Modeling MESFET's for intermodulation analysis of resistive FET mixers," in *IEEE MTT-S Int. Microwave Symp. Dig.*, June 1995, pp. 1247–1250.

[3] S. Peng, P. McCleer, and G. I. Haddad, "Intermodulation analysis of FET resistive mixers using Volterra series," in *IEEE MTT-S Int. Microwave Symp. Dig.*, June 1996, pp. 1377–1380.

[4] J. A. Garcia, J. C. Pedro, N. B. De Carvalho, A. M. Sanchez, and A. T. Puente, "Resistive FET mixer conversion loss and IMD optimization by selective drain bias," *IEEE Trans. Microwave Theory Tech.*, vol. 47, pp. 2382–2392, Dec. 1999.

[5] K. Yhland, N. Rorsman, M. Garcia, and H. F. Merkel, "A symmetrical nonlinear HFET/MESFET model suitable for intermodulation analysis of amplifiers and resistive mixers," *IEEE Trans. Microwave Theory Tech.*, vol. 48, pp. 15–22, Jan. 2000.

[6] S. Peng, P. J. McCleer, and G. I. Haddad, "Nonlinear models for the intermodulation analysis of FET mixers," *IEEE Trans. Microwave Theory Tech.*, vol. 43, pp. 1037–1045, May 1995.

[7] Y. Kwon, D. Pavlidis, P. Marsh, G. I. Ng, T. Brock, and D. C. Streit, "A miniaturized W-band monolithic dual-gate InAlAs/InGaAs HEMT mixer," in *IEEE GaAs IC Symp. Tech. Dig.*, Oct. 1993, pp. 215–218.

[8] V. Nair, S. Tehrani, R. L. Vaitkus, and D. G. Scheitlin, "Low power HFET down converter MMIC's for wireless communication applications," *IEEE Trans. Microwave Theory Tech.*, vol. 43, pp. 3043–3047, Dec. 1995.

[9] M. Nakayama, K. Horguchi, K. Yamamoto, Y. Yoshii, S. Suematsu, and T. Takagi, "A 1.9 GHz single-chip RF front-end GaAs MMIC with low-distortion cascode FET mixer for personal handy-phone system terminals," in *IEEE MTT-S Int. Microwave Symp. Dig.*, June 1998, pp. 171–174.

[10] H. I. Kang, J. H. Kim, Y. Kwon, and J. E. Oh, "An asymmetric GaAs MMIC dual-gate mixer with improved intermodulation characteristics," in *IEEE MTT-S Int. Microwave Symp. Dig.*, June 1999, pp. 795–798.

[11] S. A. Maas, *Nonlinear Microwave Circuits*. Norwood, MA: Artech House, 1988.

[12] Y. Kwon, D. Pavlidis, P. Marsh, G. I. Ng, and T. Brock, "Experimental characteristics and performance analysis of monolithic InP-based HEMT mixers at W-band," *IEEE Trans. Microwave Theory Tech.*, vol. 41, pp. 1–8, Jan. 1993.

[13] Y. Kwon, D. Pavlidis, T. Brock, and D. C. Streit, "A D-band monolithic fundamental oscillator using InP-based HEMT's," *IEEE Trans. Microwave Theory Tech.*, vol. 41, pp. 2236–2344, Dec. 1993.

[14] Y. Kwon, K. Kim, E. A. Sovero, and D. S. Deakin, "Watt-level Ka- and Q-band MMIC power amplifiers operating at low voltages," *IEEE Trans. Microwave Theory Tech.*, vol. 48, pp. 891–897, June 2000.

[15] Y. C. Chen, D. L. Lngram, H. C. Yen, R. Lai, and D. C. Streit, "A new empirical *I–V* model for HEMT devices," *IEEE Microwave Guided Wave Lett.*, vol. 8, pp. 342–344, Oct. 1988.

[16] J. C. Pedro and J. Perez, "An improved MESFET model for prediction of intermodulation load-pull characterization," in *IEEE MTT-S Int. Microwave Symp. Dig.*, June 1992, pp. 825–828.

[17] ——, "Accurate simulation of GaAs MESFET's intermodulation distortion using a new drain-source current model," *IEEE Trans. Microwave Theory Tech.*, vol. 42, pp. 25–33, Jan. 1994.

[18] C. Tsironis, R. Meirer, and R. Stahlmann, "Dual-gate MESFET mixer," *IEEE Trans. Microwave Theory Tech.*, vol. MTT-32, pp. 245–255, Mar. 1984.

[19] Y. Kwon and D. Pavlidis, "Phasor diagram analysis of millimeter-wave HEMT mixers," *IEEE Trans. Microwave Theory Tech.*, vol. 43, pp. 2165–2167, Sept. 1995.

Junghyun Kim (S'99) was born in Pusan, Korea, in 1972. He received the B.S. degree from Sung Kyun Kwan University, Seoul, Korea, in 1998, the M.S. degree in electrical engineering from Seoul National University, Seoul, Korea, in 2000, and is currently working toward the Ph.D. degree at Seoul National University.

His research is focused on MMIC design and intermodulation analysis of mixer and power amplifiers.

Youngwoo Kwon (S'90–M'94) was born in Korea, in 1965. He received the B. S. degree in electronics engineering from the Seoul National University, Seoul, Korea, in 1988, and the M.S. and Ph.D. degrees in electrical engineering from The University of Michigan at Ann Arbor, in 1990 and 1994, respectively.

From 1994 to 1996, he was with the Rockwell Science Center, where he was involved in the development of various millimeter-wave monolithic integrated circuits based on HEMTs and heterojunction bipolar transistors (HBTs). In 1996, he joined the faculty of School of Electrical Engineering, Seoul National University. His current research activities include the design of MMICs for mobile communication and millimeter-wave systems, large-signal modeling of microwave transistors, application of micromachining techniques to millimeter-wave systems, nonlinear noise analysis of MMICs, and millimeter-wave power combining.